

Multiphoton Coincidence Spectroscopy

L. Horvath, B. C. Sanders and B. F. Wielinga
*Department of Physics, Macquarie University
Sydney, New South Wales 2109, Australia*
(November 9, 2018)

We extend the analysis of photon coincidence spectroscopy beyond bichromatic excitation and two-photon coincidence detection to include multichromatic excitation and multiphoton coincidence detection. Trichromatic excitation and three-photon coincidence spectroscopy are studied in detail, and we identify an observable signature of a triple resonance in an atom-cavity system.

42.50.Ct,42.50.Dv

I. INTRODUCTION

Cavity quantum electrodynamics (CQED) [1] in the optical domain is rapidly progressing: advances in atom cooling methods, as well as improved optical cavities which allow large dipole coupling strengths, are leading experiments into new frontiers of research. Single-atom experiments are now possible [2,3], and trapping of atoms in optical cavities should soon be feasible [4]. Quantum effects and quantitative testing of theoretical models for the CQED system can be performed better than ever and perhaps directed to certain applications such as quantum logic gates [5]. Exciting developments are also taking place in the microwave domain [6–8], but here we are concerned with photon coincidence measurements, which are performed only in the optical domain.

The method of photon coincidence spectroscopy (PCS) has been introduced as a means to study the spectrum of the combined atom-cavity system [9–12], but this method was restricted to probing only the first couplet of the nonlinear regime of the Jaynes-Cummings (JC) spectrum (see Fig.1). Here we generalize the method of photon coincidence spectroscopy to show how probing of higher levels of the spectrum can be performed, and we show that three-photon coincidence spectroscopy (3PCS) could yield a signature of the second couplet in the nonlinear regime of the JC spectrum [13], thus enabling direct, unambiguous probing of the quantum features of a single atom in an optical cavity.

Photon coincidence spectroscopy is necessary to probe quantum features of the atomic CQED system because practical difficulties limit the efficacy of other techniques. The major difficulties in the optical regime include the width of the atomic beam traversing the cavity, motion of the atom through the cavity, and the interruption of the Rabi oscillation numerous times during passage through the cavity as well as a fluctuating atomic number. However, for sufficiently slow moving atoms [10], the atoms can be regarded as being essentially stationary, and the motion and spread of the atoms are responsible, then, for an inhomogeneous broadening of the spectral peaks. Furthermore, at low densities, single-atom effects dominate over multi-atom process, and the JC model provides an excellent description. Photon coincidence spectroscopy was then devised as a way to probe the interesting quan-

tum features in the presence of unavoidable inhomogeneous broadening.

Until now, only two-photon coincidence spectroscopy (2PCS) has been studied, both as quantum trajectory simulations [10] and analytic, continued-fraction methods [11,12]. However, 2PCS is only useful for probing the second couplet of the JC ladder, or, equivalently, the first couplet of the nonlinear regime (see Fig.1). Our aim here is to propose multi-photon, or N -photon coincidence spectroscopy (NPCS) as a method for probing higher-level states and to show explicitly how 3PCS would work and its feasibility.

II. DYNAMICS

The JC Hamiltonian for the atom-cavity system

$$\hat{H}(g) = \hbar\omega\hat{N} + i\hbar g\hat{A}, \quad (2.1)$$

where ω is both the atomic transition frequency and cavity resonance frequency, g is the dipole coupling strength,

$$\hat{N} = \hat{\sigma}_3 + \hat{a}^\dagger\hat{a} + 1/2 \quad (2.2)$$

is the “excitation number” operator, and

$$\hat{A} = \hat{a}^\dagger\hat{\sigma}_- - \hat{a}\hat{\sigma}_+ = -\hat{A}^\dagger, \quad (2.3)$$

describes the isolated atom-cavity system. The coupling strength g is not actually a fixed constant in the calculations: instead a distribution $P(g)$ is constructed which accounts for the variability of atomic position within the cavity mode and results in inhomogeneous broadening [10,11]. The master equation

$$\begin{aligned} \dot{\rho} = & [\hat{H}(g), \rho]/i\hbar + [\mathcal{E}(t)\hat{\sigma}_+ - \mathcal{E}^*(t)\hat{\sigma}_-, \rho] \\ & + (\gamma_I/2)(2\hat{\sigma}_-\rho\hat{\sigma}_+ - \hat{\sigma}_+\hat{\sigma}_-\rho - \rho\hat{\sigma}_+\hat{\sigma}_-) \\ & + \kappa(2\hat{a}\rho\hat{a}^\dagger - \hat{a}^\dagger\hat{a}\rho - \rho\hat{a}^\dagger\hat{a}), \end{aligned} \quad (2.4)$$

incorporates both the driving term $\mathcal{E}(t)$ and losses through the cavity mirror and by fluorescence. The solution ρ is g -dependent, and the final result for the density matrix is

$$\rho = \int P(g)\rho(g)dg \quad (2.5)$$

where $\rho(g)$ represents the solution of the master equation (2.4) for fixed g .

In order to perform NPCS, which is designed to probe the N^{th} couplet, the driving field must be N -chromatic; *i.e.*

$$\mathcal{E}(t) = \sum_{m=1}^N \mathcal{E}_m e^{-i\omega_m t} \quad (2.6)$$

for $\{\mathcal{E}_m\}$ a set of N constants, which are assumed to be real without loss of generality. Moreover, the amplitudes \mathcal{E}_m are sufficiently large to ensure significant occupation of the excited states but not so large that Stark shifts or occupation of the higher order ($n > N$) states is significant. By judicious choice of each frequency ω_m , selective excitation to the N^{th} couplet is possible.

In the rotating frame $\omega_1 = 0$, and we define detunings $\delta_m \equiv \omega_m - \omega$.

The randomness of the coupling strength $\{g\}$ is responsible for the inhomogeneous broadening depicted in Fig. 1, where g_{max} is the coupling strength between the atom and cavity mode at an antinode of the longitudinal axis. As the probability for the atom-field coupling strength being g_{max} is quite small, we choose instead to selectively excite the coupled atom-cavity system for some other $g = g_f < g_{\text{max}}$. Thus, we fix $\omega_1 = \omega + g_f$ as shown in Fig. 1, and the amplitude of this field is, of course, \mathcal{E}_1 . More conveniently, the normalized detunings are defined by

$$\tilde{\delta}_m \equiv \delta_m / g_f. \quad (2.7)$$

We also define a normalised coupling strength as $\tilde{g} = g / g_f$. The master equation (2.4) can be expressed instead in terms of the Liouville superoperator as

$$\begin{aligned} \mathcal{L}(g, t)\rho(g, t) = & \mathcal{Q}(g)\rho(g, t) + \sum_{m=2}^N \left(\mathcal{E}_m e^{-i(\delta_m - g_f)t} \Sigma_+ \right. \\ & \left. - \mathcal{E}_m^* e^{i(\delta_m - g_f)t} \Sigma_- \right) \rho(g, t) \end{aligned} \quad (2.8)$$

where $\Sigma_{\pm}\rho \equiv [\sigma_{\pm}, \rho]$, and $\mathcal{Q}(g)$ includes conservative and dissipative superoperators. The Bloch function method is applied by expanding

$$\rho(g, t) = \sum_{\vec{k} \in \mathbb{Z}^{N-1}} \rho_{\vec{k}}(g, t) e^{-i\vec{k} \cdot (\vec{\delta} - g_f \vec{1})t} \quad (2.9)$$

for \mathbb{Z}^{N-1} the set of all length $N-1$ vectors with integer values and $\vec{1}$ the vector with unity as every

*The multiphoton spectroscopic signal quality will depend on the choices of g_f ; for our simulation, we choose a value which provides a good signal but not necessarily the optimal signal.

component. Transient effects can be neglected; hence, $\lim_{t \rightarrow \infty} \dot{\rho}_{\vec{k}}(g, t) \rightarrow 0$. Thus, eq. (2.8) reduces to

$$\begin{aligned} \sum_{m=2}^N \mathcal{E}_m \left(\Sigma_+ \rho_{\vec{k} - \vec{1}_{m-1}}(g) - \Sigma_- \rho_{\vec{k} - \vec{1}_{m+1}}(g) \right) \\ + \left[i\vec{k} \cdot (\vec{\delta} - g_f \vec{1}) + \mathcal{Q}(g) \right] \rho_{\vec{k}}(g) = 0 \end{aligned} \quad (2.10)$$

where time dependence is ignored as $t \rightarrow \infty$, and $\vec{1}_m$ is a vector with all elements being 0 except the m^{th} element which is one. Writing the superoperators $\mathcal{Q}(g)$ and Σ_{\pm} as matrices and $\rho(g)$ as a vector, eq. (2.10) represents infinitely many coupled linear equations. In order to reduce the number of equations to a finite number, we introduce a positive integer q and establish the approximation

$$\rho_{\vec{k}}(g) = 0 \quad \forall \vec{k} \text{ satisfying } \sum_{i=1}^{N-1} |k_i| > q,$$

which is valid for sufficiently small $\{\mathcal{E}_k\}$. We perform our expansion in the dressed state basis $\{|n\rangle_{\pm} | n \in \{0\} \cup \mathbb{Z}^+ \}$ which satisfies

$$\hat{H}|n\rangle_{\pm} = \hbar[n\omega \pm \sqrt{n}g]|n\rangle_{\pm}, \quad \hat{H}|0\rangle = 0.$$

This spectrum of \hat{H} eigenvalues is shown in Fig. 1. For NPCS, we truncate beyond the $N+1$ couplet. Hence, each coefficient $\rho_{\vec{k}}(g)$ is of length $(1+2(N+1))^2$. Setting $q=1$ leaves $5+2(N-3)$ matrix equations, each square matrix of dimension $(1+2(N+1)) \times (1+2(N+1))$.

We are particularly interested in $\rho_{\vec{k}=\vec{0}}(g)$, which is the ‘dc’, or non-oscillating, component of the Bloch expansion. In an experiment, the N -chromatic field would drive the atom-cavity system, and N -quanta resonances would yield N -photon decays over a timescale shorter than the cavity lifetime [12]. To a good approximation, the N -photon coincidence rate is proportional to $\langle a^{\dagger N} a^N \rangle$, and we evaluate this mean with respect to the density matrix component $\rho_{\vec{k}=\vec{0}}(g)$. The elements of the density matrix are designated

$$\begin{aligned} \rho_{00}(g) & \equiv (0|\rho_{\vec{k}=\vec{0}}(g)|0), \quad \rho_{nn'}^{\varepsilon\varepsilon'}(g) \equiv \varepsilon(n|\rho_{\vec{k}=\vec{0}}(g)|n')\varepsilon', \\ \rho_{0n}^{\varepsilon}(g) & \equiv (0|\rho_{\vec{k}=\vec{0}}(g)|n)\varepsilon \equiv \rho_{n0}^{\varepsilon}(g)^*. \end{aligned} \quad (2.11)$$

The resonance would be observed in practice by fixing $\tilde{\delta}_i$ for $i=2, 3, \dots, N-1$, and varying $\tilde{\delta}_N$. The N^{th} couplet is then observable experimentally as an increase in the N -photon coincidence rate as a function of $\tilde{\delta}_N$; *i.e.* as $\langle a^{\dagger N} a^N \rangle$ vs $\tilde{\delta}_N$.

However, excited state resonances are complicated by the existence of off-resonant excitations which result in spurious N -photon decays. To study these resonant and off-resonant effects in greater detail, we calculate multiphoton peak heights at various values of $\tilde{\delta}_N$ using the non-Hermitian Hamiltonian formalism. The master equation (2.4) incorporates a non-unitary evolution which can be treated as a combination of ‘loss’ terms

and ‘jump’ terms, in the sense of quantum trajectories [10]. The non-Hermitian Hamiltonian is [12]

$$H_{\text{eff}}(g) = (\omega - \omega_1)\hat{N} + ig\hat{A} + i \sum_{m=1}^N \mathcal{E}_m(e^{-i(\delta_m - g_f)t} \sigma_+ - e^{i(\delta_m - g_f)t} \sigma_-) - \kappa a^\dagger a - (\gamma_I/2)\sigma_+\sigma_- \quad (2.12)$$

We expand the Hamiltonian as a matrix in the truncated dressed-state basis, where coefficients of states in the $(N+1)^{\text{th}}$ couplet and higher are ignored: the time-dependent state is approximated by

$$|\psi(g, t)\rangle \approx c_0(g, t)|0\rangle + \sum_{n=1}^3 \sum_{\varepsilon=\pm} c_n^\varepsilon(g, t)|n\rangle_{n\varepsilon} \quad (2.13)$$

with $\langle \psi(g, t)|\psi(g, t)\rangle \leq 1 \forall t \geq 0$ and $c_0(t=0) = 1$ and $c_n^\varepsilon(t=0) = 0$. We work in the rotating-wave approximation, and the $2N+1$ coefficients $\{c_0, \{c_n^\varepsilon\}\}$ can be written as a vector $\vec{c}(g, t)$. The matrix differential equation is $\dot{\vec{c}}(g, t) = M(g, t)\vec{c}(g, t)$. We can write the matrix as

$$M(g, t) = \sum_{\ell=0}^L M_\ell e^{-i\Omega_\ell t}, \quad (2.14)$$

where $\vec{\Omega}$ is a vector of unequally spaced discrete frequencies, ordered from $\Omega_0 = 0$ to ever-increasing values of frequency. That is, $\Omega_i > \Omega_j$ for $i > j$. In solving the equation, we ignore terms $\Omega_{\ell > L}$ where L is a cut-off parameter. Physically this corresponds to retaining terms responsible for Stark shifts in levels up to order L . Truncating this expansion is valid because we assume that the amplitudes of the driving fields $\{\mathcal{E}_m\}$ are small.

This calculation of $\{c_0, \{c_n^\varepsilon\}\}$ allows us to approximate the N -photon count rate (NPCR) $\langle a^{\dagger N} a^N \rangle$ for given values of $\tilde{\delta}_N$ where peaks are observed in the full simulation following from eq. (2.10). We use this analysis to verify the validity of the computer simulation, applied to the special case $P(g) = \delta(g - g_f)$, and to observe the importance of the Stark effect on the peak heights. As we show below for 3PCS, we have excellent agreement between numerical simulations and this semianalytic approach using the non-Hermitian Hamiltonian formalism.

III. THREE-PHOTON COINCIDENCE SPECTROSCOPY

For large N , significant computer time and memory is required to solve the equations, but 3PCS, corresponding to $N = 3$, is readily solved. To probe the third couplet of the JC ladder, a trichromatic driving field is employed. Ideally a photon of frequency $\omega_1 = \omega + g_f$ induces the transition $|0\rangle \rightarrow |1\rangle_+$, followed by another photon of frequency $\omega_2 = \omega + (\sqrt{2} - 1)g_f$ which takes the excitation

from the $|1\rangle_+$ to the $|2\rangle_+$ state, and, finally, a third photon of frequency ω_3 scans the system over a range of frequencies including the $|2\rangle_+ \leftrightarrow |3\rangle_\pm$ transitions as shown in Fig. 1.

By setting $N = 3$, eq. (2.10) reduces to

$$0 = [i(k_2\delta_2 + k_3\delta_3) + \mathcal{Q}(g)]\rho_{k_2, k_3}(g) + \mathcal{E}_2\Sigma_+\rho_{k_2-1, k_3}(g) - \mathcal{E}_2\Sigma_-\rho_{k_2+1, k_3}(g) + \mathcal{E}_3\Sigma_+\rho_{k_2, k_3-1}(g) - \mathcal{E}_3\Sigma_-\rho_{k_2, k_3+1}(g). \quad (3.1)$$

Applying the approximation $\rho_{k_2, k_3}(g) = 0$ for $|k_2| + |k_3| > q$ reduces the number of coupled matrix equations to $n(q) = 2q^2 + 2q + 1$, where coefficients corresponding to the fifth couplet and higher are ignored. Hence, there are 81 scalar coefficients of $\rho_{k_2, k_3}(g)$. In order to reduce computing time, we set $q = 1$ thereby yielding 2025 simultaneous equations.

The signature of genuine three-photon decay can be obtained by measuring the three-photon count rate (3PCR), $\langle \hat{a}^{\dagger 3} \hat{a}^3 \rangle$, vs $\tilde{\delta}_3$ to observe three-photon resonance peaks. The density matrix elements and the 3PCR are shown in Fig. 2 for a range of \tilde{g} . In Fig. 2(a) we observe two important features for ρ_{00} . Firstly, there are two valleys located at $\tilde{\delta}_3 = \pm\tilde{g}$ due to the vacuum Rabi splitting effect. Secondly, there are two valleys located at $\tilde{g} = 1$ and $\tilde{g} = \sqrt{2} - 1$, independent of $\tilde{\delta}_3$. The former valley due to off-resonant three-photon excitation to the third couplet from the ground state via the pathway $\omega_1 \rightarrow \omega_2 \rightarrow \omega_2$ (a photon with frequency ω_1 resonantly excites $|0\rangle$ to $|1\rangle_+$, followed by resonant excitation by a photon with frequency ω_2 to $|2\rangle_+$ and finally off-resonant excitation by a photon with frequency ω_2 to $|3\rangle_+$). The energy of the state $|3\rangle_+$ is $\hbar(3\omega + (2\sqrt{2} - 1)g_f)$ for $\tilde{g} = 1$. The sum of the energies in the three photons producing the $\omega_1 \rightarrow \omega_2 \rightarrow \omega_2$ off-resonant excitation pathway is $\hbar(3\omega + \sqrt{3}g_f)$. The detuning is thus $(2\sqrt{2} - 1 - \sqrt{3})g_f \doteq 0.1g_f$, which is quite small, thus ensuring the significant depletion observed in Fig. 2(a). In Fig. 2(b), where $\rho_{\frac{1}{3}\frac{1}{3}}$ is plotted, a ridge is observed at $\tilde{g} = 1$, and the off-resonant excitation to $\rho_{\frac{3}{3}\frac{3}{3}}$ is thus clear.

The second valley in Fig. 2(a) occurs at $\tilde{g} = \sqrt{2} - 1$. This depletion from the ground state arises due to resonant excitation from the ground state $|0\rangle$ to the excited state $|1\rangle_+$ via absorption of a photon of frequency ω_2 which is fixed (independent of $\tilde{\delta}_3$). In contradistinction to the presence of a ridge at $\tilde{g} = 1$ in Fig. 2(b), a ridge is *not* observed in Fig. 2(b) at $\tilde{g} = \sqrt{2} - 1$ because excitation to the second couplet is off-resonant. On the other hand excitation to the second couplet is resonant for $\tilde{g} = 1$ and so the ridge is visible for $\tilde{g} = 1$ in Fig. 2(b).

The two valleys in Fig. 2(a) at $\tilde{g} = 1$ and $\tilde{g} = \sqrt{2} - 1$ have different depths. As each valley is induced by resonant excitation from $|0\rangle$ to $|1\rangle_+$, the depletion of ρ_{00} can be calculated from a two-state approximation [11,14]

$$\rho_{00} \doteq 1 - \frac{\mathcal{E}_m^2}{\frac{1}{2}(\kappa + \gamma_I/2)^2 + 2\mathcal{E}_m^2}, m = 1, 2.$$

For $\tilde{g} = 1$, $m = 1$ and $\mathcal{E}_1 = 1/\sqrt{2}$ producing $\rho_{00} \doteq 13/17$ as observed in Fig. 2(a). Similarly, for $\tilde{g} = \sqrt{2} - 1$, $m = 2$ and $\mathcal{E}_2 = \sqrt{2}$ producing $\rho_{00} \doteq 25/41$ which again matches Fig. 2(a).

A subtle feature of Fig. 2(b) is the presence of two dips along the ridge at $\tilde{g} = 1$. One dip occurs at $\tilde{\delta}_3 = -1$. This dip is due to competition between two excitation pathways. One path involves resonant excitation via the ω_1 photon to $|1\rangle_+$, and the second path is resonant excitation to $|1\rangle_-$ via the ω_3 photon. Excitation to $|1\rangle_-$ diminishes the probability of excitation to $|1\rangle_+$ which is necessary for the $\omega_1 \rightarrow \omega_2 \rightarrow \omega_2$ off-resonant excitation to $|3\rangle_+$, hence the dip in ρ_{33}^{++} .

The second dip occurs at $\tilde{\delta}_3 = -(\sqrt{2} + 1)$ which also occurs due to competition between paths; however, this dip is less noticeable. Both paths experience resonant excitation to $|1\rangle_+$, but the ω_3 photon excites to $|2\rangle_-$ in competition with the $\omega_2 \rightarrow \omega_2$ two-photon subsequent excitation to $|3\rangle_+$. As the competition occurs for electrons in the $|1\rangle_+$ state, instead of for the $|0\rangle$ state in the case of the other dip, the competition, and hence the dip, is less significant.

Two prominent off-resonant peaks are centred about $(\tilde{\delta}_3, \tilde{g}) = (1, 1)$ and the other at $(\tilde{\delta}_3, \tilde{g}) = ((\sqrt{2} - 1)^2, \sqrt{2} - 1)$. The former peak is due to cooperative excitation pathways via the three-photon excitations $\omega_1 \rightarrow \omega_2 \rightarrow \omega_2$ and $\omega_3 \rightarrow \omega_2 \rightarrow \omega_2$. The equality between ω_3 and ω_1 is responsible for this cooperative effect. The second off-resonant peak is due to cooperation between the pathways $\omega_2 \rightarrow \omega_2 \rightarrow \omega_2$ and $\omega_2 \rightarrow \omega_3 \rightarrow \omega_3$. The ridge at $\tilde{g} = \sqrt{2} - 1$ due to the $\omega_2 \rightarrow \omega_2 \rightarrow \omega_2$ pathway is, however, negligible due to off-resonant excitation to the second couplet as well as to the third couplet.

There is a prominent peak at $(\tilde{\delta}_3, \tilde{g}) = (\sqrt{3} - \sqrt{2}, 1)$ in Fig. 2(a), corresponding to cooperative excitation pathways $\omega_1 \rightarrow \omega_2 \rightarrow \omega_3$ and $\omega_1 \rightarrow \omega_3 \rightarrow \omega_2$ for resonant excitation to $|3\rangle_+$. The off-resonant excitation pathway $\omega_1 \rightarrow \omega_2 \rightarrow \omega_2$ also occurs.

Finally, we observe a peak for $\tilde{g} \leq 0.1$ and centred at $\tilde{\delta}_3 = 0$. This peak is very large near $\tilde{g} = 0$ (not shown) and corresponds to very small splitting of the couplets. Consequently, the system behaves much like a decoupled atom and cavity and acts as a resonator for $\tilde{\delta}_3 = 0$. The 3PCR, proportional to $\langle a^{\dagger 3} a^3 \rangle$, is plotted in Fig. 2(c). The similarity between Figs. 2(b) and 2(c) is evidence that occupation of $|3\rangle_+$ is a good indicator of the 3PCR. However, occupation of $|3\rangle_-$ also contributes to the 3PCR. The peak at $\tilde{\delta}_3 = -(\sqrt{3} + \sqrt{2})$ in Fig. 2(c) is due to the excitation pathway $\omega_1 \rightarrow \omega_2 \rightarrow \omega_3$ which resonantly excites to $|3\rangle_-$. The peak at $\tilde{\delta}_3 = -(\sqrt{3} + \sqrt{2})$ is somewhat diminished, however, by the off-resonant $\omega_1 \rightarrow \omega_2 \rightarrow \omega_2$ excitation pathway. The peak at $\tilde{g} \leq 0.1$ is significantly larger in Fig. 2(c) than in Fig. 2(b) due to contributions from off-resonant excitation to both $|3\rangle_-$ and $|3\rangle_+$.

The peaks, valleys and ridges in Figs. 2 have been explained in terms of excitation pathways. We have intro-

duced each of these pathways by studying the system intuitively, but a verification is possible using the effective non-Hermitian Hamiltonian (2.12) and the approximate time-dependent unnormalized state (2.13). In Table I we presented analytical estimates of the 3PCR $\langle a^{\dagger 3} a^3 \rangle_{\text{est}}$, using the non-Hermitian Hamiltonian, and compare to the 3PCR, $\langle a^{\dagger 3} a^3 \rangle$, observed in Fig. 2(c). Although the estimates can vary from the observed 3PCR by up to a factor of 2.5, the agreement is excellent considering that ‘jump’ terms have been ignored which significantly decrease the peak height. An exception is the dip at $(\tilde{\delta}_3, \tilde{g}) = (-1, 1)$ where the ‘jump’ terms are responsible for an increase in peak height. Table I provides confirmation of the pathways suggested as being responsible for features in Figs. 2. In each case the cut-off parameter is $L = 1$, except for $\tilde{\delta}_3 = -(\sqrt{3} + \sqrt{2})$ where $L = 2$ is due to two pathways: one resonantly exciting to $|3\rangle_-$ and the other due to off-resonant excitation to $|3\rangle_+$.

In Figs. 3(a) and 3(b) we present the 3PCR *vs* $\tilde{\delta}_3$, averaged over $P(g)$, assuming a TEM₀₀ mode in the cavity and a mask for the atomic beam. The expression for $P(g)$ is complicated and is provided in the appendix of Ref. [11]. The average 3PCR is thus

$$\overline{\langle a^{\dagger 3} a^3 \rangle} = \int \text{Tr}(\rho(g) a^{\dagger 3} a^3) P(g) dg. \quad (3.2)$$

Fig. 3(a) corresponds to a strong coupling of $g_f/\kappa = 63$. This strong coupling ensures that fine features are not destroyed by inhomogeneous broadening. By comparison, the case $g_f/\kappa = 9$ is presented in Fig. 3(b), and the deleterious effects of inhomogeneous broadening are evidently much stronger for the weaker-coupling case.

In each graph the dotted line corresponds to the 3PCR *after* background subtraction. To perform background subtraction, the experiment is performed four times, once with all three fields on and scanned over $\tilde{\delta}_3$. The experiment is then repeated for the three cases (i) $\mathcal{E}_1 = \mathcal{E}_2 = 0$, (ii) $\mathcal{E}_1 \neq 0$ and $\mathcal{E}_2 = 0$ and (iii) $\mathcal{E}_1 = 0$ and $\mathcal{E}_2 \neq 0$. The contribution to the 3PCR is then due solely to the excitations by (i) ω_3 photons, (ii) ω_1 and ω_3 photons, and (iii) ω_2 and ω_3 photons. Case (i) is a subset of (ii) and (iii), hence must be subtracted from (ii) and (iii). Using the notation of Ref. [11], we denote the spectrum after subtraction as

$$\Delta^{(3)}(\tilde{\delta}_3) \equiv \overline{\langle a^{\dagger 3} a^3 \rangle}(\tilde{\delta}_3) - \overline{\langle a^{\dagger 3} a^3 \rangle}_{\mathcal{E}_1=0}(\tilde{\delta}_3) - \overline{\langle a^{\dagger 3} a^3 \rangle}_{\mathcal{E}_2=0}(\tilde{\delta}_3) + \overline{\langle a^{\dagger 3} a^3 \rangle}_{\mathcal{E}_1=0, \mathcal{E}_2=0}(\tilde{\delta}_3). \quad (3.3)$$

In Fig. 3, the value of background subtraction is apparent. The 3PCR for the strong-coupling case $g_f/\kappa = 63$, depicted in Fig. 3(a), is improved by background subtraction. Broadening about $\tilde{\delta}_3 = 0$ is reduced, and the peak at $\tilde{\delta} = \sqrt{3} - \sqrt{2}$ is more evident after background subtraction. Furthermore, the multiple peak structure near $\tilde{\delta}_3 = 0$, before background subtraction, consists of undesirable off-resonant contributions. These are effectively removed by background subtraction, and the dip

in the 3PCR at $\tilde{\delta}_3 = 1$ is evident. The reason for this dip is that $\omega_3 = \omega_1$, and the two pathways $\omega_1 \rightarrow \omega_2 \rightarrow \omega_2$ (which is responsible for the background 3PCR, independent of the value of $\tilde{\delta}_3$) and $\omega_3 \rightarrow \omega_2 \rightarrow \omega_2$ are complementary. Of course the most important peak occurs at $\tilde{\delta} = -(\sqrt{3} + \sqrt{2})$, which is outside the inhomogeneous broadening region. Observing this peak would not require the time-consuming background subtraction methods necessary for discerning the other peaks. This peak at $\tilde{\delta}_3 = -(\sqrt{3} + \sqrt{2})$ exhibits the desired “ $\sqrt{3}$ ” signature for excitation to the third couplet as well as the “ $\sqrt{2}$ ” signature arising from the excitation from the second couplet.

One of the finer features in Fig. 3(a) is the dip at $\tilde{\delta}_3 = -1$. This dip is due to the significant dip in Fig. 2(c) for $(\tilde{\delta}_3, \tilde{g}) = (-1, 1)$. However, the size of the dip is somewhat reduced due to a very small peak at $(\tilde{\delta}_3, \tilde{g}) = (-1, \sqrt{2}-1)$ in Fig 2(c) due to the off-resonant excitation pathway $\omega_2 \rightarrow \omega_3 \rightarrow \omega_1$ to $|3\rangle_+$. Although this peak is quite small, $P(g)$ is more highly weighted for low g .

For Fig. 3(a) the strong coupling case $g_f/\kappa = 63$ has been adopted. The importance of strong coupling is that homogeneous broadening due to widths $\gamma_I/2$ and κ are small, and contributions due to off-resonant transitions are less significant. In previous analyses of PCS, albeit for the two-photon case, the coupling strength $g_f/\kappa = 9$ has been adopted. For 3PCS, such a coupling is too small. In Fig. 3(b) some of the more dramatic features of Fig. 3(a) are still discernible but degraded to a level of near indistinguishability from the background. We observe the dips at $\tilde{\delta} = \pm 1$ and the (very broad) peak at $\tilde{\delta} = -(\sqrt{3} + \sqrt{2})$. However, experimental observation of such features is unlikely, and a higher coupling strength is desirable. A coupling strength of $g_f/\kappa = 63$ is not required, but a coupling strength higher than $g_f/\kappa = 9$ is necessary.

IV. CONCLUSION

The technique of photon coincidence spectroscopy (PCS) has been extended from driving the atom-cavity coupled system by a bichromatic field and measuring two-photon coincidences [9–12] to multichromatic driving fields and multichromatic coincidences. Whereas two-photon coincidence spectroscopy (2PCS) enables observation of the $2\sqrt{2}g$ splitting of the spectrum, associated with the second couplet, higher-order photon coincidence spectroscopy allows direct probing of higher couplets in the JC ladder. This technique thus offers a valuable tool for resolving higher-order spectral phenomena in cavity quantum electrodynamics. Although the focus here has been on an atomic beam and the spectrum associated with the JC ladder, this scheme can be adapted to studying spectra of other cavity QED systems with a discrete spectrum and significant inhomogeneous broadening.

We can also see that off-resonant phenomena are increasingly important for probing higher-order couplets. The background subtraction scheme is more intricate. Also resolving peaks for higher-order couplets requires increasingly large coupling strengths. The required coupling strength places a bound on the feasibility of N -photon coincidence spectroscopy, and we see that a large coupling strength is required even for $N = 3$.

ACKNOWLEDGEMENT

We have benefited from valuable discussions with H. J. Carmichael, Z. Ficek and K.-P. Marzlin. This research has been supported by a Macquarie University Research Grant and by an Australian Research Council Small Grant.

-
- [1] *Cavity Quantum Electrodynamics*, edited by P. R. Berman (Academic Press, Boston, 1993).
 - [2] C. J. Hood, M. S. Chapman, T. W. Lynn and H. J. Kimble, Phys. Rev. Lett. **80**, 4157 (1998).
 - [3] H. Mabuchi, J. Ye and H. J. Kimble, J. Appl. Phys. B (1998).
 - [4] K. S. Wong, M. J. Collet and D. F. Walls, Opt. Commun. **137**, 269 (1997).
 - [5] Q. A. Turchette, C. J. Hood, W. Lange, H. Mabuchi and H. J. Kimble, Phys. Rev. Lett. **75**, 4710 (1995).
 - [6] M. Brune, F. Schmidt-Kaler, A. Maali, J. Dreyer, E. Hagley, J. M. Raimond, and S. Haroche, Phys. Rev. Lett. **76**, 1800 (1996).
 - [7] S. Haroche, M. Brune and J. M. Raimond, Phil. Trans. R. Soc. London. A **355**, 2367 (1997).
 - [8] X. Maitre, E. Hagley, J. Dreyer, A. Maali, C. Wunderlich, M. Brune, J. M. Raimond and S. Haroche, J. Mod. Opt. **44**, 2023 (1997).
 - [9] B. C. Sanders and H. J. Carmichael, CLEO/Pacific Rim '95: The Pacific Rim Conference on Lasers and Electro-Optics Technical Digest (Makuhari Messe Convention Center, July 10-14, 1995), pp 243-4.
 - [10] H. J. Carmichael, P. Kochan, and B. C. Sanders, Phys. Rev. Lett. **77**, 631 (1996).
 - [11] B. C. Sanders, H. J. Carmichael and B. F. Wielinga, Phys. Rev. A **55**, 1358 (1997).
 - [12] L. Horvath, B. C. Sanders and B. F. Wielinga, APS Eprint: aps1998may26_001.
 - [13] E. T. Jaynes and F. W. Cummings, Proc. IEEE **51**, 89 (1963).
 - [14] L. Tian and H. J. Carmichael, Phys. Rev. A **46**, R681 (1992).

FIG. 1. A three-photon excitation scheme from the ground state $|0\rangle$ to the first three couplets $|n\rangle_\epsilon$ ($n \leq 3$) of the dressed states with inhomogeneously broadened energy bands.

FIG. 2. Plots of (a) ρ_{00} , (b) ρ_{33}^{++} and (c) the $\langle a^{\dagger 3} a^3 \rangle$ vs normalised scanning field frequency, $\tilde{\delta}_3$, and coupling strength, \tilde{g} , for $\gamma_I/\kappa = 1$, $g_f/\kappa = 63$, $\mathcal{E}_1/\kappa = 1/\sqrt{2}$ and $\mathcal{E}_2/\kappa = \mathcal{E}_3/\kappa = \sqrt{2}$.

FIG. 3. Plots of $\langle a^{\dagger 3} a^3 \rangle$ with (solid) and without (dots) background subtraction vs $\tilde{\delta}_3/\pi$ for $\gamma_I/\kappa = 1$, $\mathcal{E}_1/\kappa = 1/\sqrt{2}$, $\mathcal{E}_2/\kappa = \mathcal{E}_3/\kappa = \sqrt{2}$ averaged over $P(g)$ for randomly-placed atom in the TEM₀₀ mode for (a) $g_f/\kappa = 63$ and (b) $g_f/\kappa = 9$.

\tilde{g}	$\tilde{\delta}_3$	$\langle a^{\dagger 3} a^3 \rangle$	$\langle a^{\dagger 3} a^3 \rangle_{\text{est}}$
$(\sqrt{2} - 1)$	$(\sqrt{2} - 1)^2$	1.2×10^{-3}	3.1×10^{-3}
1	1	1.7×10^{-3}	1.7×10^{-3}
1	$\sqrt{3} - \sqrt{2}$	1.5×10^{-3}	2.6×10^{-3}
1	-1	2.4×10^{-4}	2.1×10^{-4}
1	$-(\sqrt{2} + 1)$	3.3×10^{-4}	3.3×10^{-4}
1	$-(\sqrt{3} + \sqrt{2})$	1.3×10^{-3}	2.1×10^{-3}

TABLE I. Three-photon count rate (3PCR) $\langle a^{\dagger 3} a^3 \rangle$ and approximate 3PCR $\langle a^{\dagger 3} a^3 \rangle_{\text{est}}$ calculated via the non-Hermitian Hamiltonian formalism.

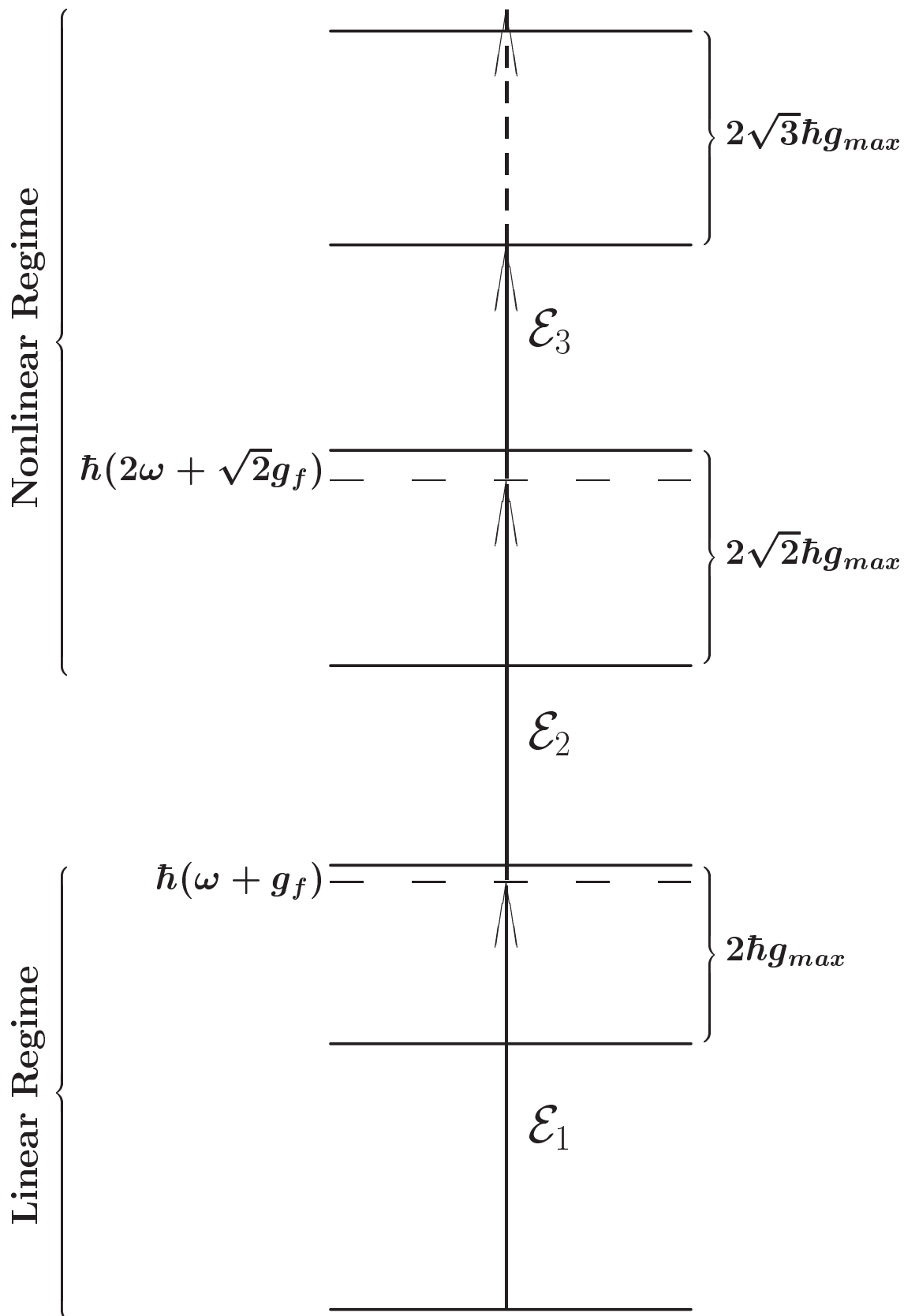
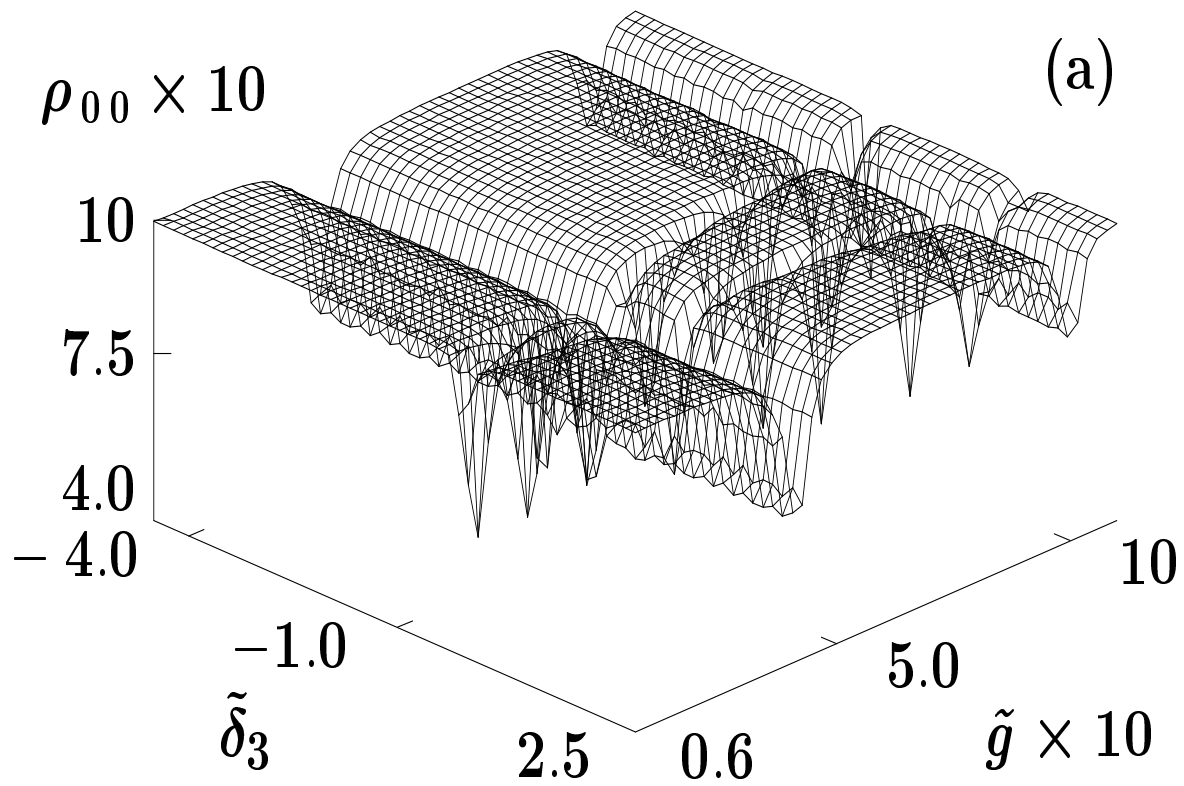


Fig. 1
 Horvath et al.
 J.Opt.B:
 Quant.Sem.Opt.



(a)

Fig. 2(a)
Horvath et al
J.Opt.B:
Quant.Sem.Opt.

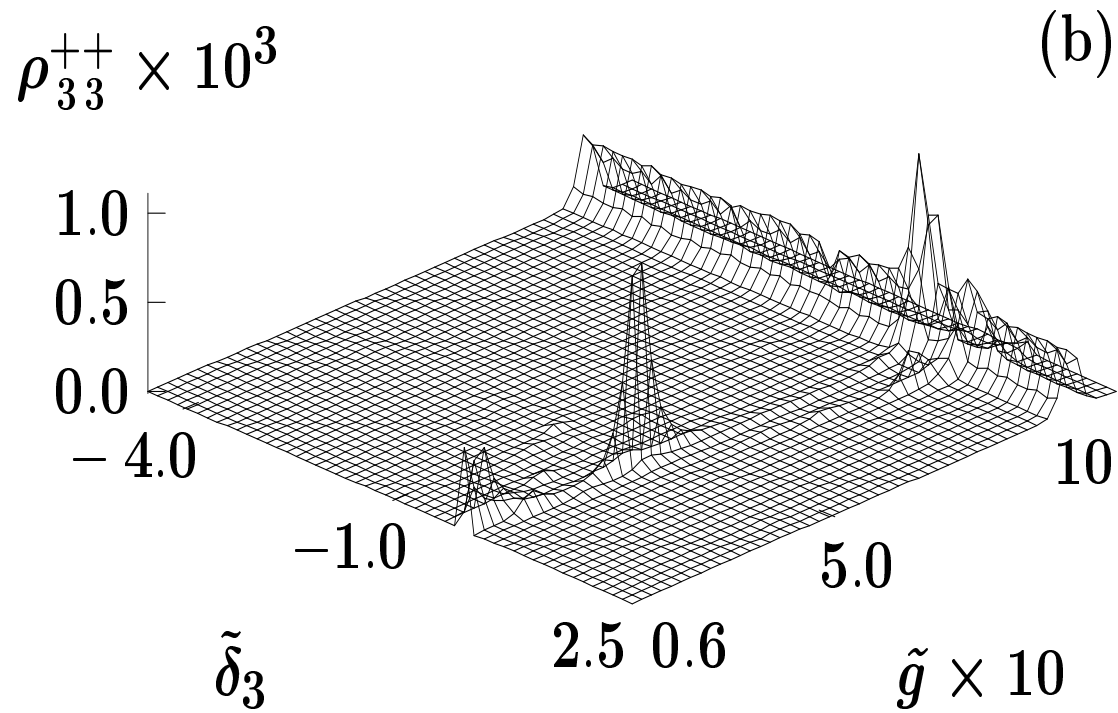


Fig. 2(b)
Horvath et al
J.Opt.B:
Quant.Sem.Opt.

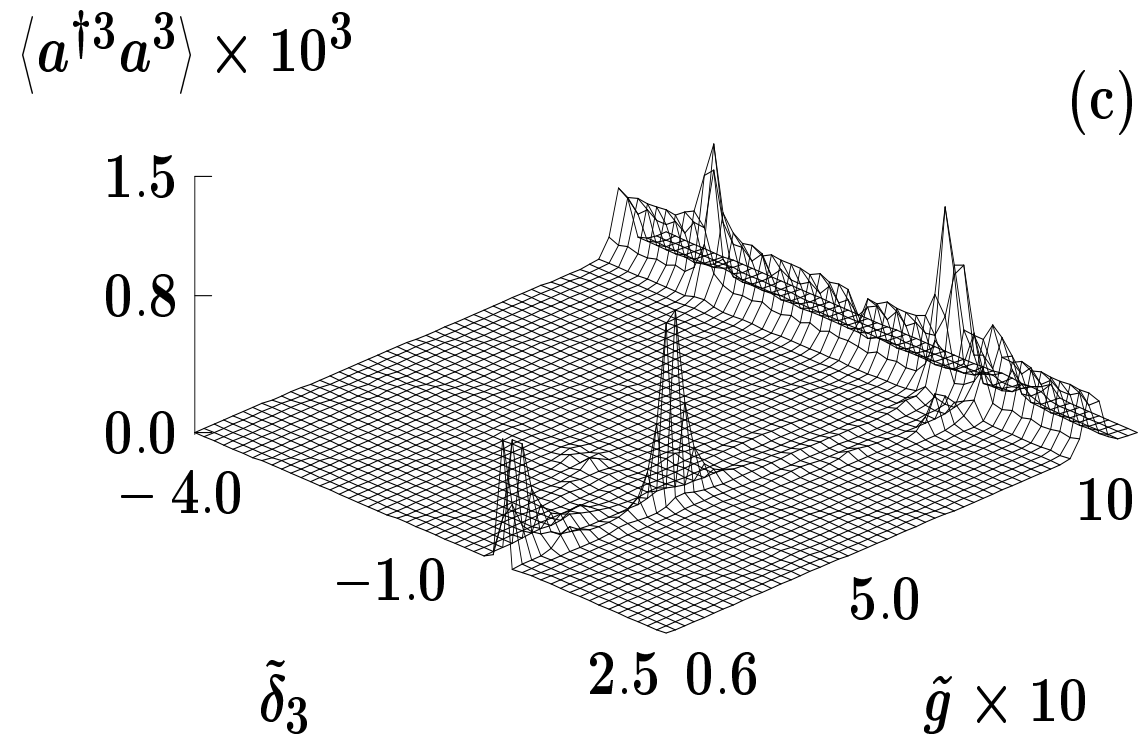


Fig. 2(c)
Horvath et al
J.Opt.B:
Quant.Sem.Opt.

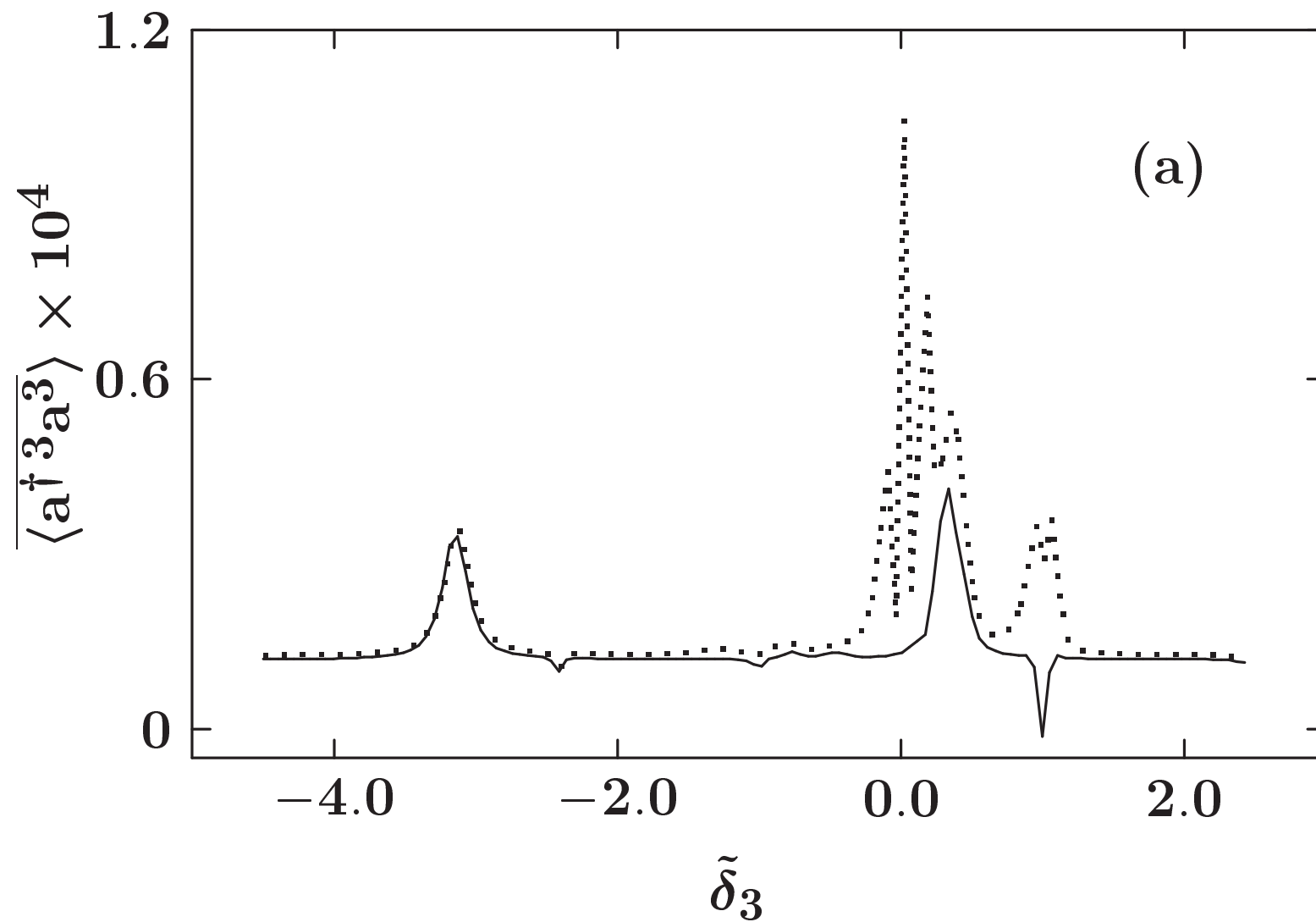


Fig. 3(a)
Horvath et al
J.Opt.B:
Quant.Sem.Opt.

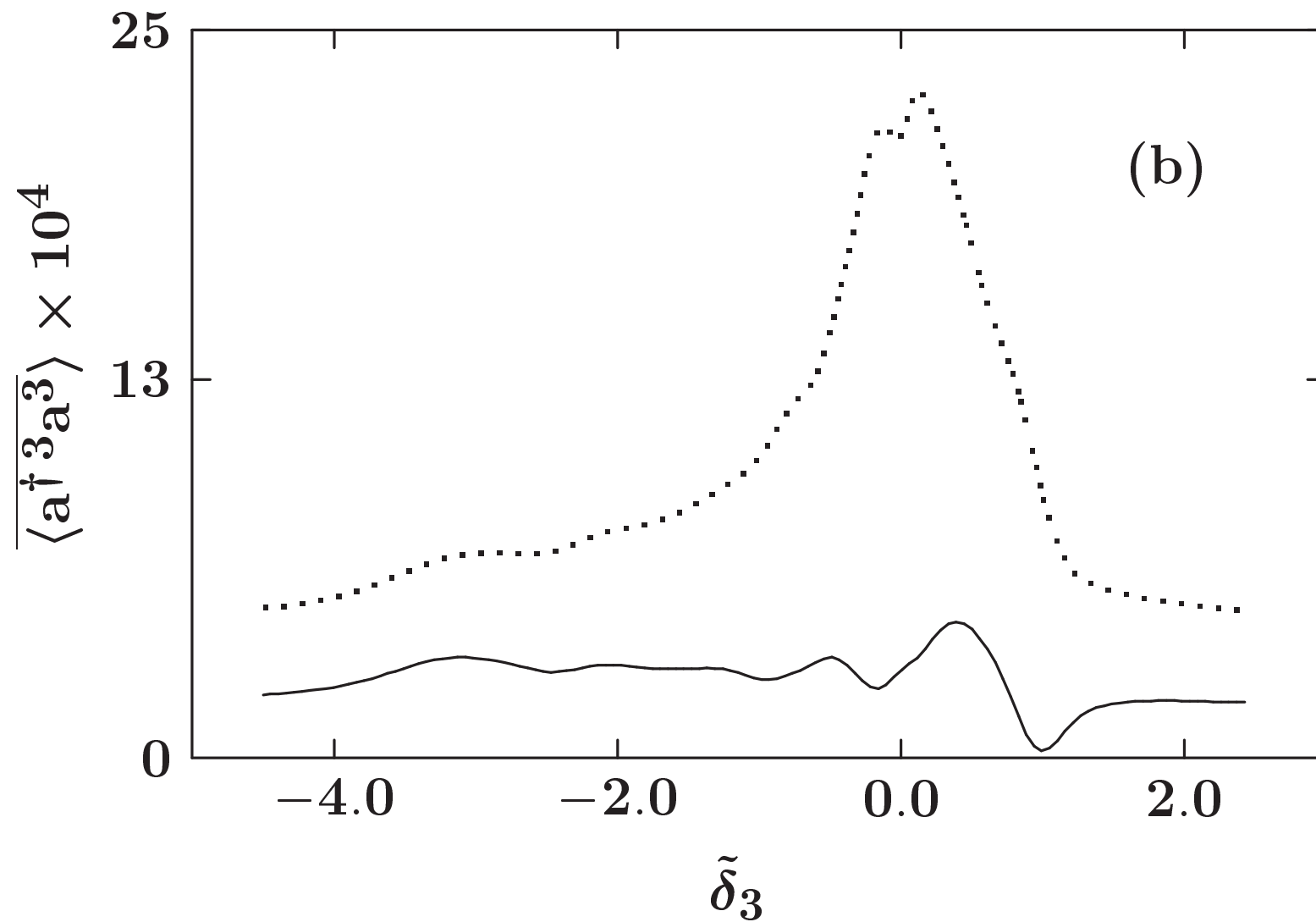


Fig. 3(b)
Horvath et al
J.Opt.B:
Quant.Sem.Opt.